Improved PWM Control With Wide Speed Range for a Double-Side Asynchronous Rotor AFPMM Series-End Winding Drive

Rundong Huang, *Member, IEEE*, and Chunhua Liu, *Senior Member, IEEE*

***Abstract*—Robot dogs are welcomed widely in industry and daily life. To reduce the volume and weight of robot dogs, a double-side asynchronous rotor axial-flux permanent magnet machine is designed for them. It has two asynchronous rotors on two sides which are driven respectively by two sets of windings, so the control of the machine is different from that of conventional machines. Thus, an improved pulsewidth modulation (PWM) control is proposed for the machine. In the control, the two sets of three-phase windings are connected in series, so there are seven legs in the drive. Compared with two separate conventional series-end winding (SEW) drives for two sides, the proposed SEW serves as a reduced-switch-count topology. Besides, it guarantees wide speed ranges for the dual rotors of the machine. Due to the overmodulation, zero sequence component (ZSC) optimization is conducted for the drive. The control scheme adopts an optimal ZSC for the dual windings with the consideration of both reference voltages of two sides. The experiment validates that the proposed improved PWM control gets better permanence compared with other methods.**

***Index Terms*—Dual winding control, improved pulsewidth modulation (PWM), reduced-switch-count topology, wide speed range, zero sequence component (ZSC) optimization.**

I. INTRODUCTION

As A new kind of mobile tool, robot dogs are applied widely in express delivery and community patrol. It needs two motors for a leg to achieve complex actions, so a double-side asynchronous rotor (DSAR) axial-flux permanent magnet machine (AFPMM) is designed to replace the two motors with smaller volume and weight [1]. It has two rotors driven by two sets of three-phase winding respectively on the two sides. There is magnetic isolation between the two sides of the DSAR-AFPMM.

Thus, the control of the DSAR-AFPMM is different from that of conventional machines. It is similar to the control of two different motors due to two sets of windings. For two different machines, conventional control methods need two drive systems. The two drive systems are separate and independent of each other.

However, in the case of open-circuit faults in inverter legs, a fault-tolerant operation is necessary. Then, for dual-motor systems, the reduced-switch-count voltage-source inverter (VSI) topology is investigated [2], [3], [4], [5]. In the dual-motor system, the two motors usually share a common leg in the drive [6], [7], [8]. In order to avoid the conflict of switching state demands between two motors, the switching period is divided into two parts for the two motors [9]. In each half period, only one motor is modulated, while the voltage of the other motor is zero. This means that the dc bus voltage utilization is only 50% of the original utilization. Then, a master-slave selection principle for two motors is adopted to overcome coupling in [10]. The selection standard is the current error of the coupling phase. [11] even proposes a general pulsewidth modulation (PWM) for a $(2n+1)$-leg VSI which supplies n machines. It is also applicable to dual-motor systems. In addition, a sensorless control is proposed for a dual-motor system [12]. The high-frequency signals are injected in the half period when the voltage is zero, so the filter for demodulation is eliminated. Furthermore, a predictive control method is designed for the overmodulation of dual-motor systems [13]. It considers different overmodulation cases and gives corresponding modulation strategies.

In these topologies, the three-phase windings in each motor all adopt the star connection. Compared with series-end winding (SEW) drives, star-connected winding drives naturally have limited dc bus voltage utilization [14], [15]. The voltage utilization of the SEW drive is closely related to the winding connection sequence for multiphase machines [16]. The SEW drives are studied and controlled in [17], [18], and [19], but they all make use of the space vector PWM (SVPWM) method. However, with more drive legs, the SVPWM method for the SEW drive is more complex due to the increasing number of voltage vectors. Hence, a carrier-based PWM method can be applied if the relationship between the phase voltage and leg voltage is determined [20], [21].

In order to enlarge the speed range for two rotors, this article adopts a seven-leg SEW drive for the DSAR-AFPMM as a fault-tolerant operation. The two sets of windings share a common leg in the drive, so an improved PWM control is proposed to deal with the conflict of switching states. It optimizes the zero

---

Received 10 November 2023; revised 19 February 2024, 7 May 2024, and 24 July 2024; accepted 9 September 2024. Date of publication 12 September 2024; date of current version 12 December 2024. This work was supported in part by the Natural Science Foundation of China under Project 52077186, in part by the Science Technology and Innovation Committee of Shenzhen Municipality, Shenzhen, China, under Project JCYJ20210324134005015, and in part by RGC Research Fellow Scheme (RGC Ref. No.: RFS2223-1S05) from Research Grants Council, Hong Kong SAR. Recommended for publication by Associate Editor T. Shi. *(Corresponding author: Chunhua Liu.)*

The authors are with the Shenzhen Research Institute, City University of Hong Kong, Hong Kong, and also with the School of Energy and Environment, City University of Hong Kong, Hong Kong (e-mail: rundonghuang@my.cityu.edu.hk; chunliu@cityu.edu.hk).

Color versions of one or more figures in this article are available at https://doi.org/10.1109/TPEL.2024.3460670.

Digital Object Identifier 10.1109/TPEL.2024.3460670

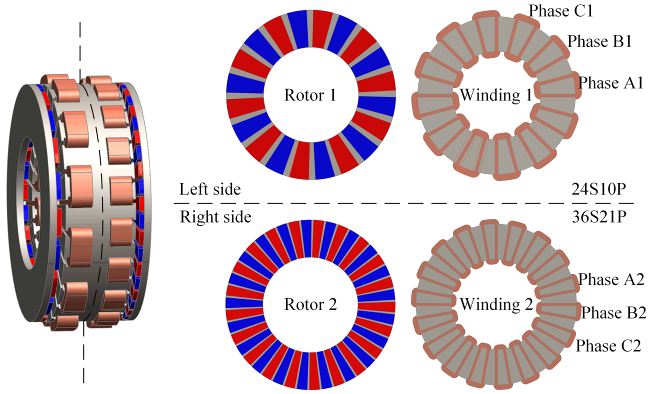

Fig. 1. DSAR-AFPMM topology.

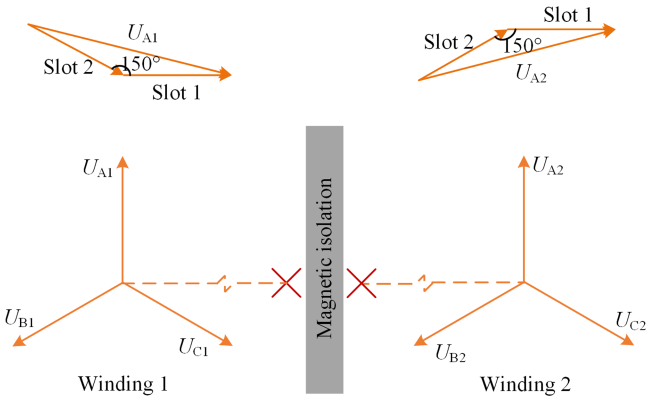

Fig. 2. Voltage phasors of dual windings.

sequence component (ZSC) to reallocate the duty cycle of each switch according to the cost function when the conflict occurs between dual windings. The cost function takes the reference voltages of dual windings into consideration simultaneously, so it meets both requirements of dual windings. In this article, the topologies of the DSAR-AFPMM and the corresponding SEW drive are introduced. Then, the PWM control strategy for the drive is illustrated. The dc bus voltage utilization is analyzed. In Section IV, the optimal ZSC for each drive leg is derived based on the cost function. In Section V, an experiment is conducted for the control scheme to validate the wide speed range of two rotors of the DSAR-AFPMM. Finally, Section VI concludes this article.

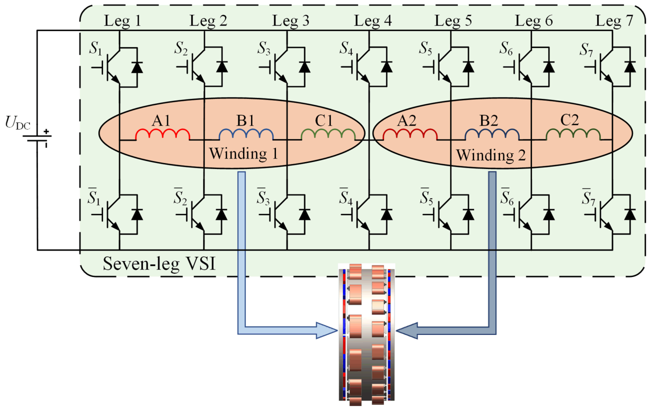

Fig. 3. SEW drive topology.

II. DSAR-AFPMM SEW Drive System

A. DSAR-AFPMM Topology

The DSAR-AFPMM is composed of one stator and two rotors. Besides, there are two sets of three-phase winding arranged on the stator. The machine mainly serves as an actuator in robot dogs. Robot dogs need two freedoms for each leg, so the two rotors of the DSAR-AFPMM have to work independently. Then, they are driven by the two sets of windings, respectively.

Fig. 1 shows the topology of the DSAR-AFPMM. The configurations on the two sides are different. On the left side, the machine has 24 slots and 10 pole pairs. On the right side, the machine has 36 slots and 21 pole pairs. Thus, the arrangements of dual windings are different on two sides. Fig. 2 shows the voltage phasors of dual windings. According to [22], the dual windings are isolated by the stator yoke, as well as the two rotors, so the neutral points of dual windings are not connected. The two rotors are also not connected to one shaft. Hence, the two rotors of the DSAR-AFPMM have to be controlled separately. Due to the magnetic isolation between the two sides, they are controlled as common three-phase machines.

B. SEW Drive Topology

Conventional star-connected winding drives have limited dc bus voltage utilization, so a SEW drive is designed for the DSAR-AFPMM to improve the voltage utilization and enlarge the speed range. Then, for the open-circuit fault in the inverter leg, a seven-leg VSI is proposed to ensure the normal operation of the machine. Fig. 3 shows the SEW drive topology for the DSAR-AFPMM.

In the drive, dual windings are connected in series. leg 1; leg 2; and leg 3 are connected to the phases of winding 1, while leg 5, leg 6, and leg 7 are connected to the phases of winding 2. Besides, leg 4 is the common leg and connected to both Phase C1 of winding 1 and phase A2 of winding 2. In the operation, phase C1 and phase A2 may have different voltage requirements for leg 4, but the two phase voltages can be adjusted arbitrarily through the voltages of leg 3, leg 4, and leg 5. There is a limit to operation only in overmodulation. The switching state will conflict between dual windings in the common leg when the overmodulation occurs. The phase voltage is calculated as

$$\begin{bmatrix} u_{A1} \\ u_{B1} \\ u_{C1} \\ u_{A2} \\ u_{B2} \\ u_{C2} \end{bmatrix} = U_{DC} \begin{bmatrix} 1 & -1 & 0 & 0 & 0 & 0 & 0 \\ 0 & 1 & -1 & 0 & 0 & 0 & 0 \\ 0 & 0 & 1 & -1 & 0 & 0 & 0 \\ 0 & 0 & 0 & 1 & -1 & 0 & 0 \\ 0 & 0 & 0 & 0 & 1 & -1 & 0 \\ 0 & 0 & 0 & 0 & 0 & 1 & -1 \end{bmatrix} \begin{bmatrix} S_1 \\ S_2 \\ S_3 \\ S_4 \\ S_5 \\ S_6 \\ S_7 \end{bmatrix}. \tag{1}$$

There are seven legs in the drive, so there are totally $2^7 = 128$ switching states. It means that the space vector selection will be very complex and the computational burden will be large if the SVPWM method is applied to the VSI. However, the PWM method does not need space vectors. It only focuses on the duty cycle of each leg. Therefore, the PWM method is very suitable for the seven-leg VSI.

III. PWM Control Strategy

A. Machine Model

For the DSAR-AFPMM, the mathematical models of the two sides need to be derived respectively, so they are similar to the model of a three-phase electric machine. Take one side as an example, the relationship between the electromagnetic torque and rotary speed is as follows:

$$T_{em} = J\frac{d\omega_m}{dt} + T_l + \mu_f \omega_m \tag{2}$$

where J is the moment of inertia of the corresponding rotor, T_{l} is the load torque, ω_m is the mechanical rotary speed, and μ_f is the friction coefficient. For different rotors, the parameters J and μ_f are different. When the rotor rotates at a constant speed, the electromagnetic torque has to be balanced with the load torque. According to the electromagnetic relationship in the machine, the electromagnetic torque is determined by the flux linkage and current. It is expressed as

$$T_{em} = \frac{3}{2}\left[p\psi i_q + p\left(L_d - L_q\right) i_d i_q\right] \tag{3}$$

where p is the pole pair number of the corresponding rotor, i_d and i_q are the *d*/*q*-axis currents, L_d and L_q are the *d*/*q*-axis inductances of corresponding winding, and ψ is the flux linkage. The *d*/*q*-axis currents can be obtained as (4) directly through the *d*/*q*-axis voltage in the synchronous rotation coordinate system because the parameters are decoupled after the Park transformation

$$\begin{bmatrix} u_d \\ u_q \end{bmatrix} = \begin{bmatrix} R_s & -\omega_e L_q \\ \omega_e L_d & R_s \end{bmatrix} \begin{bmatrix} i_d \\ i_q \end{bmatrix} + \begin{bmatrix} L_d & 0 \\ 0 & L_q \end{bmatrix} \begin{bmatrix} di_d/dt \\ di_q/dt \end{bmatrix} + \begin{bmatrix} 0 \\ \omega_e \psi \end{bmatrix} \tag{4}$$

where R_s is the resistance, u_d and u_q are the *d*/*q*-axis voltages, and ω_e is the electrical rotary speed. The transformation from phase voltages to the *d*/*q*-axis voltages is shown as (5). At first, the phase voltages u_A, u_B, and u_C have to be converted to u_α and u_β in the stationary coordinate system. Then, the *d*/*q*-axis voltages are calculated with the electrical angle θ_e of the rotor

$$\begin{bmatrix} u_d \\ u_q \end{bmatrix} = \begin{bmatrix} \cos\theta_e & -\sin\theta_e \\ \sin\theta_e & \cos\theta_e \end{bmatrix} \begin{bmatrix} u_\alpha \\ u_\beta \end{bmatrix} \tag{5}$$

$$\begin{bmatrix} u_\alpha \\ u_\beta \end{bmatrix} = \frac{2}{3}\begin{bmatrix} 1 & \cos\frac{2\pi}{3} & \cos\frac{4\pi}{3} \\ 0 & \sin\frac{2\pi}{3} & \sin\frac{4\pi}{3} \end{bmatrix} \begin{bmatrix} u_A \\ u_B \\ u_C \end{bmatrix}. \tag{6}$$

The machine model is adopted for both sides of the DSAR-AFPMM with different parameters. Based on the model, the electromagnetic torque and rotary speed are both related to the voltage. So, a wide speed range of the rotor can be obtained if a high voltage is provided to the corresponding winding.

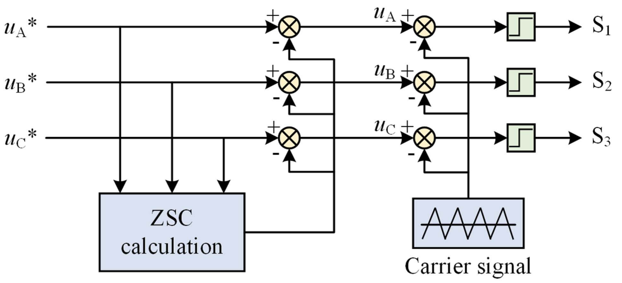

Fig. 4. Structure of conventional carrier-based PWM.

B. PWM Method

Fig. 4 shows the structure of a carrier-based PWM for a conventional three-phase star-connected winding VSI. It includes a ZSC injection to increase the dc bus voltage utilization. The modulating signals are compared with the high-frequency carrier signal to generate switching signals. In the VSI, the switching signal of each leg is only determined by the corresponding phase voltage, so the switching signals of all the legs have certain values when the reference phase voltages are calculated.

In the SEW drive, the relationship between leg voltages and phase voltages is different from that in the star-connected winding drive. It is shown in (7), where $k = 1, 2, \ldots, 7$, $ph = \mathrm{A, B, C}$. The leg voltage is proportional to the duty cycle of the leg in the VSI, so the positive pulsewidth has to be calculated according to the reference phase voltage

$$u_{ph} = u_{lk} - u_{l(k+1)} = U_{\mathrm{DC}}\left(t_{lk} - t_{l(k+1)}\right). \tag{7}$$

It can be seen from (7) that one phase voltage is dependent on the two adjacent leg voltages. There are seven legs for the two sets of three-phase windings in the SEW drive. Thus, the seven-leg voltages are still uncertain even when all the phase voltages are acquired. It is assumed that the first leg voltage is equal to the last leg voltage in [20]. Then, the leg voltages are calculated through several transformations, which increases the computational burden of the controller.

In this article, the leg voltages do not need to be calculated. The duty cycle of each leg is calculated directly. According to the above analysis, there are many possibilities for the leg voltages when the phase voltages are given. It also means that all the duty cycles are not certain. Thus, the unit voltage of the first leg can be set to 1 as a reference. Then, the unit value of each phase voltage is calculated as (8), where v_{11} is equal to 1

$$v_{ph} = u_{ph}/U_{\mathrm{dc}} = v_{lk} - v_{l(k+1)}. \tag{8}$$

The unit value of phase voltage is also the difference in voltages between two legs. Therefore, the unit voltages of the rest legs can be obtained with the reference. In order to increase the dc bus voltage utilization, an appropriate ZSC is injected to modulate the signal. In this way, the reference phase voltages can also be obtained. Fig. 5 shows the structure of the proposed carrier-based PWM.

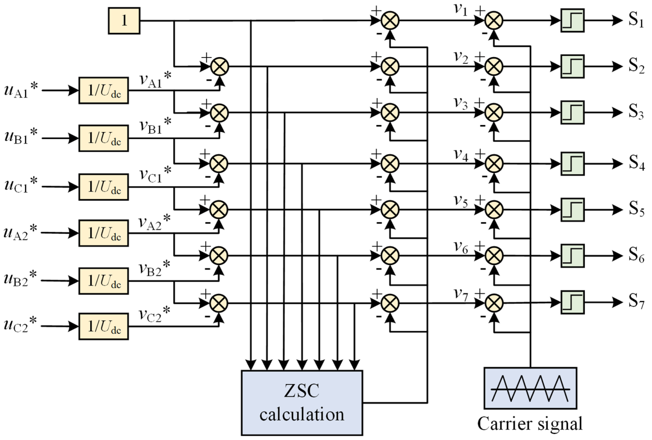

Fig. 5. Structure of proposed carrier-based PWM.

C. DC-Bus Voltage Utilization

It is obvious that the SEW drive has higher dc bus voltage utilization than the star-connected winding drive. However, in the seven-leg VSI, the dc-bus voltage utilization is closely related to the connection of dual windings. It is also defined in [23] that the modulation index M is the ratio of the peak value of phase voltage to half of the dc bus voltage. The phase voltage of the machine can be expressed as

$$u_{ph} = U_{ph} \sin(\omega_e t + \varphi) = M \frac{U_{dc}}{2} \sin(\omega_e t + \varphi). \quad (9)$$

For the first four legs in the drive, the peak value of the voltage between any two legs will not be larger than that of phase voltage. For example, the amplitude of the voltage between leg 1 and leg 3 is still $MU_{dc}/2$ shown in (10). It is also the same for the last 4 legs. Thus, it is important to study the effect of the connection between the two sets of windings

$$\begin{aligned} u_{13} &= u_{A1} + u_{B1} \\ &= M\frac{U_{dc}}{2}\sin(\omega_e t) + M\frac{U_{dc}}{2}\sin\left(\omega_e t + \frac{2\pi}{3}\right) \\ &= M\frac{U_{dc}}{2}\sin\left(\omega_e t + \frac{\pi}{3}\right) \end{aligned} \quad (10)$$

$$\begin{cases} u_{35} = u_{C1} + u_{A2} \\ u_{36} = u_{C1} + u_{A2} + u_{B2} = u_{C1} - u_{C2} \\ u_{25} = u_{B1} + u_{C1} + u_{A2} = u_{A2} - u_{A1} \\ u_{26} = u_{B1} + u_{C1} + u_{A2} + u_{B2} = -u_{A1} - u_{C2} \end{cases}. \quad (11)$$

The connection between dual windings is shown in (11). All the voltages should be smaller than the dc bus voltage. The phase and frequency of phase voltages between dual windings may both be different, so (12) has to be met to get the linear modulation region

$$M_1\frac{U_{dc}}{2} + M_2\frac{U_{dc}}{2} \le U_{dc} \quad (12)$$

where M_1 and M_2 are the modulation indexes of the two sets of windings, respectively. According to (12), the sum of the two modulation indexes cannot exceed 2. The linear modulation region of the proposed SEW drive is much larger than that of the star-connected winding drive in [11]. The sum of the modulation indexes is 1.73 times of that in the star-connected winding drive. A larger linear modulation region means higher dc bus voltage utilization. Therefore, the drive can provide a wide speed range for the two rotors.

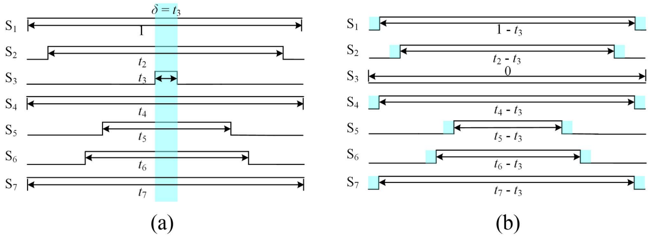

Fig. 6. Switching pattern of the drive. (a) Without ZSC injection. (b) With ZSC injection.

IV. ZSC OPTIMIZATION

In a conventional star-connected drive, the leg voltage in the carrier-based PWM control is expressed as (13). It is usually composed of two parts. One is the sinusoidal component v^*_{lk}, the other is the ZSC v_{l0}

$$v_{lk} = v^*_{lk} + v_{l0}. \quad (13)$$

In the proposed PWM method, the first part in (13) may not only contain a sinusoidal component but also contain a ZSC. However, according to (7), all the ZSCs are eliminated in the calculation of phase voltages, so it will not affect the operation of the machine. If there is no overmodulation, the ZSC v_{l0} in the SEW drive can be obtained as (14). It is the negative minimum value among all the leg voltages

$$v_{l0} = -\min\left(v^*_{l1}, v^*_{l2}, \ldots, v^*_{l7}\right). \quad (14)$$

Then, the switching pattern for the DSAR-AFPMM is shown in Fig. 6. Fig. 6(a) shows the switching pattern without zero sequence injection. The blue region is the instant when all the legs are switched on. It is reduced by injecting ZSC into leg voltages. After the ZSC injection, all the duty cycles are changed. The minimum value is 0 as shown in Fig. 6(b).

With the ZSC injection, the modulation signals of the seven legs can be obtained in a simulation. In this normal condition, the two rotors run at 400 and 300 r/min, respectively. The carrier frequencies for the seven legs are the same. Fig. 7 shows the modulation signals. The value means the time the leg switches ON. Then, the switching pattern of the drive is determined and phase voltages are obtained. Different from conventional modulation signals, they are not saddle-shaped after the ZSC injection. The reason is that the ZSC suitable for one set of winding is applied to all legs. It makes the modulation signals for the other set of winding not regular, but they do not affect the work. The modulation signal of the common leg also does not need additional treatment in normal conditions.

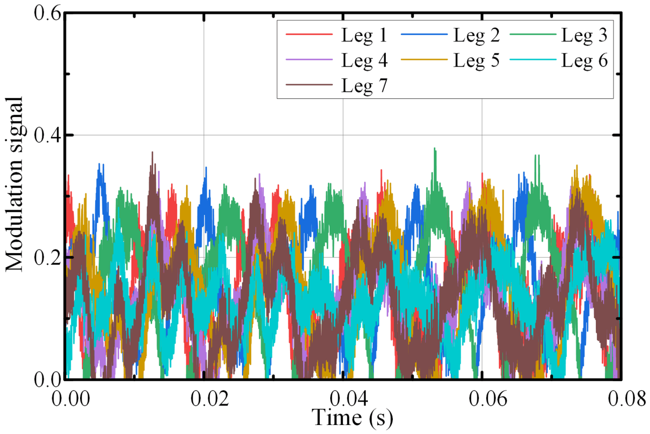

Fig. 7. Modulation signals of all drive legs in the simulation.

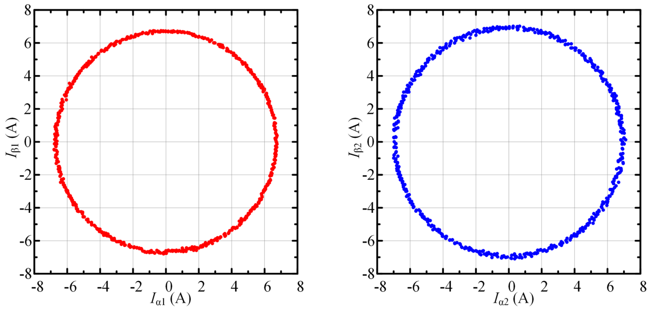

(a)

(b)

Fig. 8. Currents i_α and i_β of the two sets of windings. (a) Winding 1. (b) Winding 2.

Fig. 8 shows the currents of the two sets of windings in the cartesian coordinate system. The waveform of the current i_α and i_β can represent the trajectory of the magnetomotive force (MMF) of the winding in the coordinate system. It can be seen that the two sets of windings both have rotational MMFs with different speeds. It means the method does not affect the normal work of the two rotors.

However, the duty cycle of some switches will exceed 1 during the overmodulation even after the ZSC injection. Thus, the switching pattern cannot be obtained directly during the overmodulation. The injected component of each switch has to be optimized to make the obtained voltages close to the reference voltages. Then, a cost function for the system can be expressed as (15) where the subscripts 1 and 2 represent winding 1 and winding 2, respectively, the superscript *ref* represents the reference voltages

$$f = \left(u_{\alpha 1} - u_{\alpha 1}^{\mathrm{ref}}\right)^2 + \left(u_{\beta 1} - u_{\beta 1}^{\mathrm{ref}}\right)^2 + \left(u_{\alpha 2} - u_{\alpha 2}^{\mathrm{ref}}\right)^2 + \left(u_{\beta 2} - u_{\beta 2}^{\mathrm{ref}}\right)^2 \tag{15}$$

$$\begin{cases} u_{\alpha 1}^{\mathrm{ref}} = \frac{2}{3} U_{\mathrm{DC}} \left(v_{l1}^* - \frac{3}{2} v_{l2}^* + \frac{1}{2} v_{l4}^*\right) \\ u_{\alpha 1} = \frac{2}{3} U_{\mathrm{DC}} \left(\left(v_{l1}^* + \delta_1\right) - \frac{3}{2}\left(v_{l2}^* + \delta_2\right) + \frac{1}{2}\left(v_{l4}^* + \delta_4\right)\right) \end{cases} \tag{16}$$

TABLE I

OVERMODULATION CONDITIONS

Condition	Duty cycles of Winding 1 and 2
I	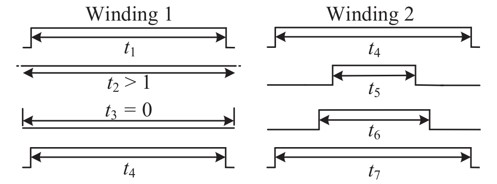
II	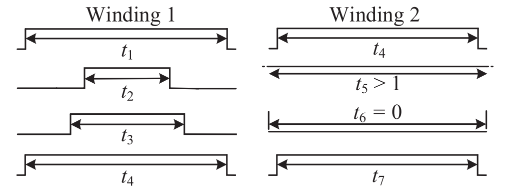
III	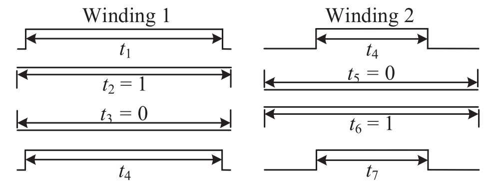
IV	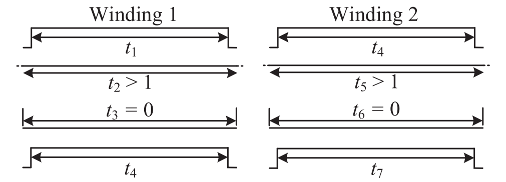

$$f = \frac{1}{9} U_{\mathrm{dc}}^2 (-2\delta_1 + 3\delta_2 - \delta_4)^2 + \frac{1}{3} U_{\mathrm{dc}}^2 (-\delta_2 + 2\delta_3 - \delta_4)^2 + \frac{1}{9} U_{\mathrm{dc}}^2 (-2\delta_4 + 3\delta_5 - \delta_7)^2 + \frac{1}{3} U_{\mathrm{dc}}^2 (-\delta_5 + 2\delta_6 - \delta_7)^2. \tag{17}$$

According to (1), (6), and (13), the reference voltage ${u_{\alpha 1}}^{\mathrm{ref}}$ and actual voltage $u_{\alpha 1}$ can be expressed as (16), where $\delta_{1,2,\ldots,7}$ is the unit value of the injected component for drive legs. The other voltages in (15) can be derived similarly. Thus, the cost function can be simplified to (17).

There are several overmodulation conditions listed in Table I for the machine. Under conditions I and II, only windings 1 and 2 are overmodulated, respectively. Under condition III, windings 1 and 2 are not overmodulated, but the overmodulation will occur when the same ZSC is injected for both windings. Condition IV is that windings 1 and 2 are both overmodulated.

A. *Condition I and II*

Under condition I, winding 2 is not overmodulated, so δ_4, δ_5, δ_6, and δ_7 are equal. Due to the same reason, δ_1, δ_2, δ_3, and δ_4 are also equal under condition II. Thus, the ZSC optimization for the two conditions is similar. Condition I is taken as an example in this article.

The sum of phase voltages of three-phase winding is assumed to be 0, so the leg voltages of leg 1 and leg 4 are the same. Then, the cost function can be written as (18). Fig. 9 shows the variation

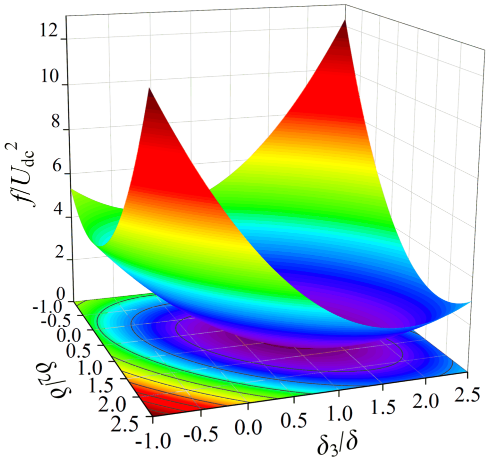

Fig. 9. Cost function with δ_2 and δ_3.

of the cost function with the reallocated duty cycles δ_2 and δ_3

$$f = \frac{1}{9}U_{\rm dc}^2(-3\delta + 3\delta_2)^2 + \frac{1}{3}U_{\rm dc}^2(-\delta_2 + 2\delta_3 - \delta)^2. \quad (18)$$

The cost function only has one minimum value. The function characteristic will not change although the leg voltages of leg 1 and leg 4 may not be the same. Thus, the optimal ZSCs δ_1, δ_2, and δ_3 can be calculated as (19). It is obvious that the cost function gets the minimum value of 0 when they are all equal to δ. However, the value cannot be obtained simultaneously in the feasible domain when winding 1 is overmodulated

$$\begin{cases} \frac{\partial f}{\partial \delta_1} = 0 \\ \frac{\partial f}{\partial \delta_2} = 0 \\ \frac{\partial f}{\partial \delta_3} = 0 \end{cases} \Rightarrow \begin{cases} \delta_1 = \frac{3}{2}\delta_2 - \frac{1}{2}\delta \\ \delta_2 = \frac{1}{3}\delta_1 + \frac{2}{3}\delta_3 \\ \delta_3 = \frac{1}{2}\delta + \frac{1}{2}\delta_2 \end{cases}. \quad (19)$$

According to Fig. 7, the injected ZSC for another two legs should be close to the results in (19) after it for one leg is determined. Thus, the injected ZSC for one leg should be determined firstly according to the original voltage. Then, the other two ZSCs can be discussed to reduce the cost function as much as possible. If the results in (19) are in the feasible region, they can be adopted. Otherwise, the boundaries of the feasible regions should be applied as the ZSC.

B. Condition III

Condition III is a special condition. Under this condition, the two sets of winding are not overmodulated if the modulation is separated. However, requirements of the two sets of windings for the duty cycle of common leg conflict. If the modulation of one side is satisfied in priority, the other side of the DSAR-AFPMM will have a bad performance.

Thus, the modulation of the two sets of winding needs to take a compromise based on the cost function. The modulation voltage of the common leg should make the cost function the smallest. It is assumed that in the separated modulation the injected ZSC of winding 1 is $\delta_{\rm I}$, while that of winding 2 is $\delta_{\rm II}$. Then, the modulation of the common leg is different from the separated modulation while that of other legs remains the same in the compromise. Hence, the cost function for the system under condition III can be expressed as (20). After the derivation, the value of δ can be obtained according to (21). It is the average value of $\delta_{\rm I}$ and $\delta_{\rm II}$

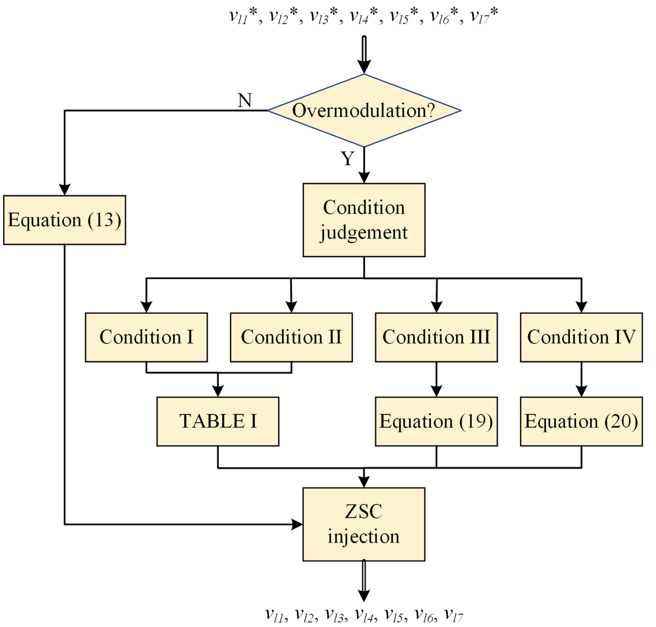

Fig. 10. Flowchart of ZSC injection.

$$f = \frac{4}{9}U_{\rm dc}^2(\delta_I - \delta)^2 + \frac{4}{9}U_{\rm dc}^2(\delta_{II} - \delta)^2 \quad (20)$$

$$\frac{\partial f}{\partial \delta} = 0 \Rightarrow \delta = \frac{\delta_I + \delta_{II}}{2}. \quad (21)$$

C. Condition IV

Under condition IV both windings 1 and 2 are overmodulated. There are too many factors that affect the cost function. It is hard to find a set of optimal ZSCs for the seven legs. Then, the modulated voltage $v_{\rm lk}$ of each leg has to be obtained after scaling down the original leg voltage $v^*_{\rm lk}$. The ZSC of all legs can be calculated as (22) where $v_{\rm lmin}$ and $v_{\rm lmax}$ are the minimum and maximum values of original leg voltages, respectively,

$$v_{l0} = -\frac{v_{l\,\rm min}}{v_{l\,\rm max} - v_{l\,\rm min}}. \quad (22)$$

Therefore, the flowchart of the ZSC injection in the improved PWM control is shown in Fig. 10. When the overmodulation occurs the condition has to be judged according to the above analysis. The corresponding ZSC is calculated and injected. Then, the SEW drive can be controlled according to Fig. 11. There are one speed loop and one current loop for each set of windings. The output of the speed regulator is the input of the current controller. The zero-sequence current is suppressed through the proportional resonant controller, while other currents are controlled through the proportional integer controller. In addition, the transformations of currents for two sets of windings are independent.

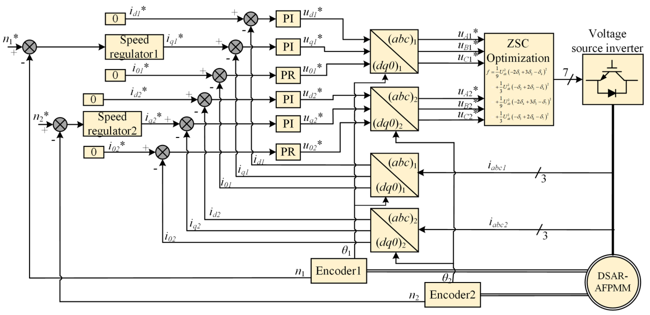

Fig. 11. Control diagram.

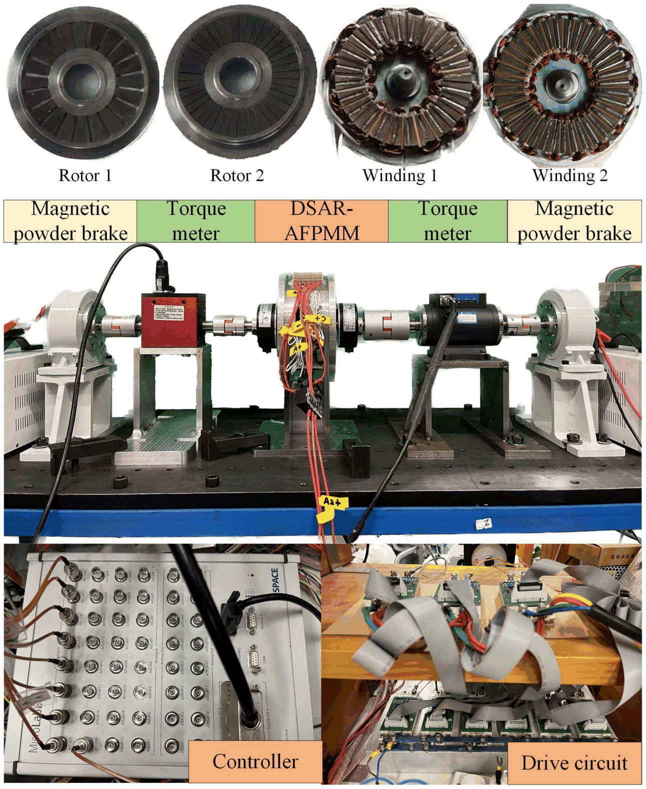

Fig. 12. Prototype components and experimental platform.

TABLE II
PARAMETERS OF THE DSAR-AFPMM AND DRIVE

Items	Description	Value
p_1	Pole pair number of Rotor 1	10
p_2	Pole pair number of Rotor 2	21
R_1	Resistance of Winding 1	0.20 Ω
R_2	Resistance of Winding 2	0.19 Ω
L_{d1}	d-axis inductance of Winding 1	0.45 mH
L_{q1}	q-axis inductance of Winding 1	0.45 mH
L_{d2}	d-axis inductance of Winding 2	0.33 mH
L_{q2}	q-axis inductance of Winding 2	0.33 mH
ψ_1	Flux linkage of Winding 1	0.014 Wb
ψ_2	Flux linkage of Winding 2	0.006 Wb
U_{dc}	DC-bus voltage	20 V
f_s	Sampling frequency	10 kHz
P_{em}	Rated power on each side	250 W
T_{em}	Rated torque of two rotors	1 Nm

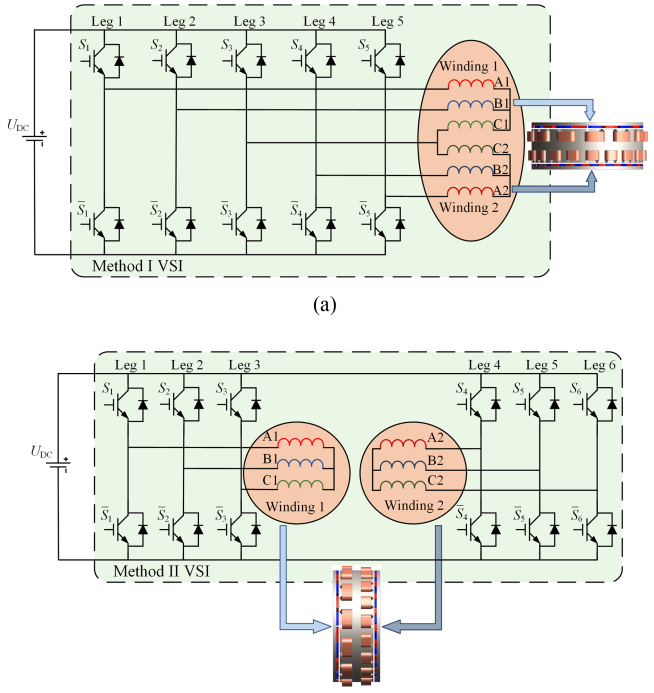

(a)

(b)

Fig. 13. Drive circuits of methods I and II. (a) Method I. (b) Method II.

V. EXPERIMENTAL VALIDATION

Fig. 12 shows the prototype components and experimental platform for the improved PWM control method. It is composed of the DSAR-AFPMM, a controller, and a drive circuit. It can be seen the two rotors are assembled on the two sides. They are connected with two rotary shafts, respectively. The two rotors of the DSAR-AFPMM are connected to two magnetic powder brakes which serve as loads. The controller is the dSPACE DS1202. The parameters of the DSAR-AFPMM and drive are given in Table II.

In order to validate the performance of the improved PWM control, this article compares it with three control methods. In method I, the two sets of winding are both star-connected, but phase C1 and phase C2 share a common leg in the drive, as shown in Fig. 13(a). Then, they are controlled through the PWM method in [11]. In method II the two sets of winding are also star-connected, but they do not share any common leg. They are controlled independently with the conventional PWM method. The drive circuit is shown in Fig. 13(b). Method III adopts the SEW drive topology shown in Fig. 3. However, the ZSC in the PWM control will be calculated as (22) under all the overmodulation conditions. Method IV is the proposed improved PWM control method. In all control methods, the DSAR-AFPMM works under the same loads. Both loads for the two rotors are 1 N·m.

A. Rotor 2 at Low Speed

The speed ranges of one rotor is affected by the speed of another rotor due to the common leg in the drive. Thus, the

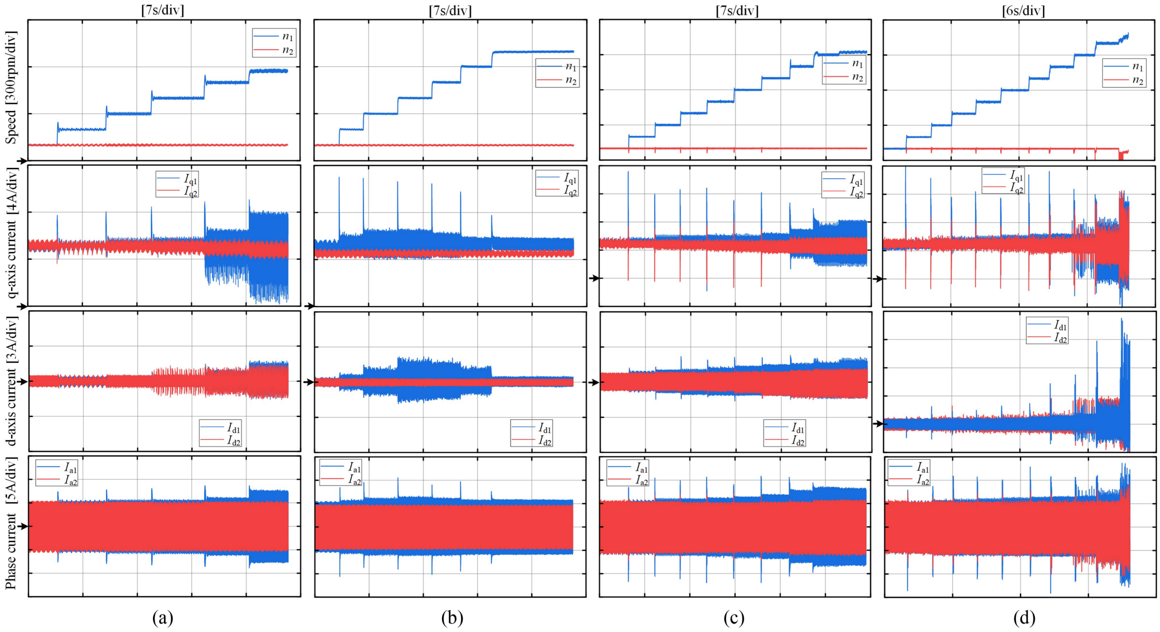

(a) (b) (c) (d)

Fig. 14. Increase in speed of rotor 1 when rotor 2 runs at 100 r/min. (a) Method I. (b) Method II. (c) Method III. (d) Method IV.

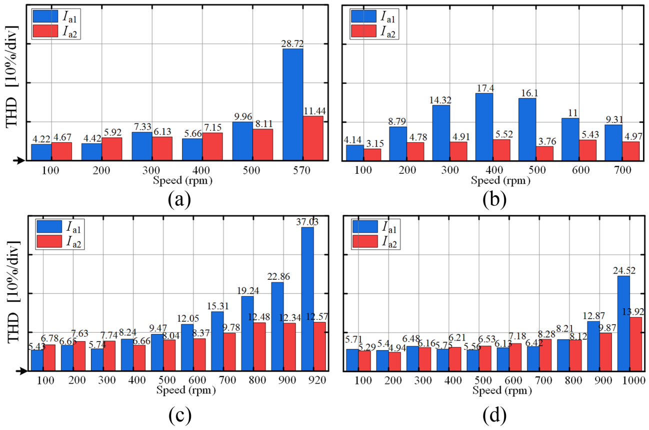

Fig. 15. THD of phase currents when rotor 2 runs at 100 r/min. (a) Method I. (b) Method II. (c) Method III. (d) Method IV.

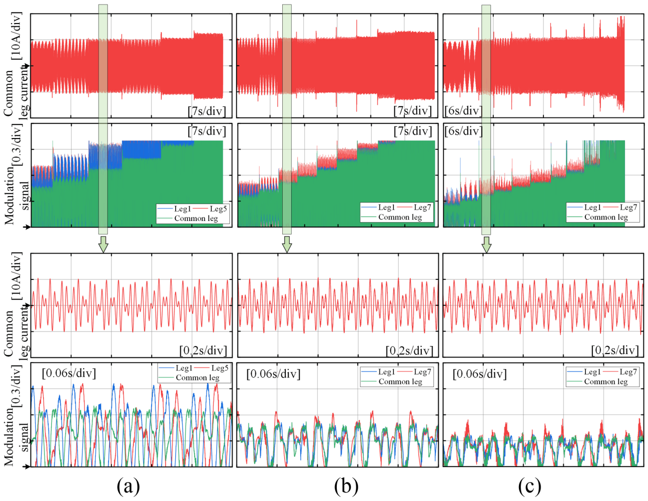

Fig. 16. Common leg currents and modulation signals when rotor 2 runs at 100 r/min. (a) Method I. (b) Method III. (c) Method IV.

speed of one rotor should be kept constant when the speed range of another rotor is measured. At first, the speed range of rotor 1 is tested when rotor 2 is at low speed. Fig. 14 shows the speeds and currents of the DSAR-AFPMM when rotor 2 runs at 100 r/min. In the measurement, the speed of rotor 1 is increased by 100 r/min at each step until the maximum. When the modulation achieves the limitation, the speed of rotor 1 cannot increase. The maximum speed of rotor 1 reflects the dc bus voltage utilization. In this case, the maximum speed of rotor 1 is 570 r/min in method I. It has the smallest speed range. In method II, the speed range of rotor 1 is not related to rotor 2. The maximum speed of rotor 1 is nearly 700 r/min. In method III, the maximum speed of rotor 1 is 920 r/min. In method IV, the speed of rotor 1 can reach 1000 r/min. The actual speed cannot follow the control when the reference speed continues increasing. The current also becomes uncontrollable. Besides, the speed of rotor 2 cannot be maintained. It means the proposed method improves the dc-bus voltage utilization. As for the current spikes, they are mainly caused by suppressing the speed spikes. It can be seen that the current spikes are smaller when the speed spikes are larger at the transient response.

Based on the Park transformation, the *d*/*q*-axis currents are calculated with the measured phase currents. With the increase of the speed, the *d*/*q*-axis current ripples become larger. It means there are more harmonics in the phase current. The total harmonic distortions (THDs) of phase currents at each speed in the four methods are shown in Fig. 15. It increases with the rotor speed in methods I, III, and IV, but the THD in method II

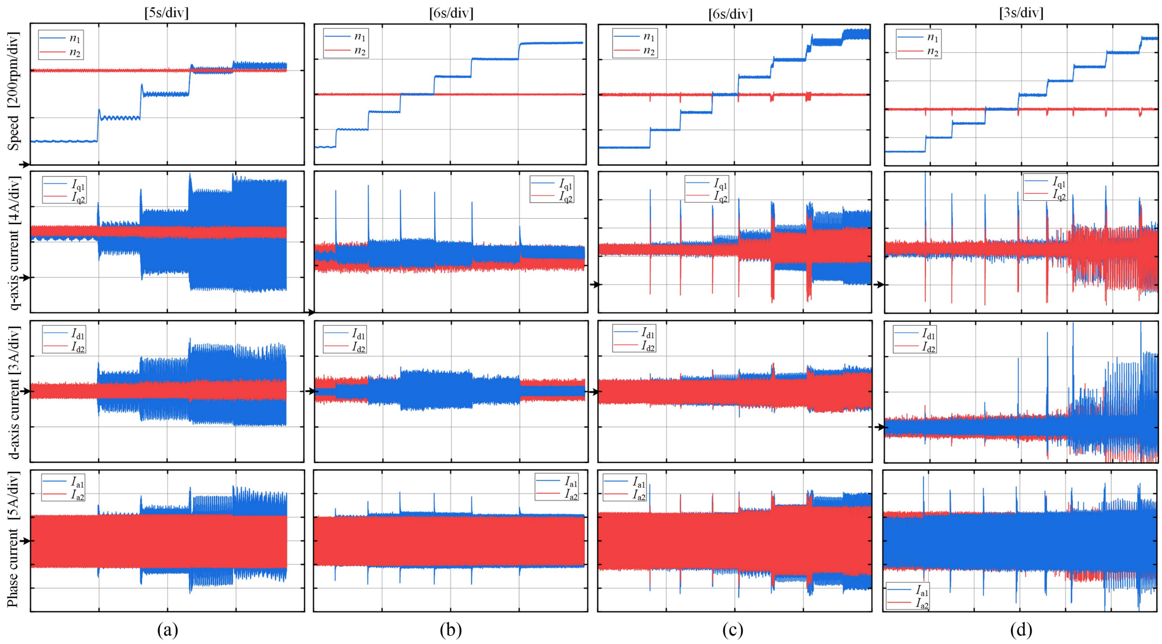

(a) (b) (c) (d)

Fig. 17. Increase in speed of rotor 1 when rotor 2 runs at 400 r/min. (a) Method I. (b) Method II. (c) Method III. (d) Method IV.

does not have the trend. The reason is that high speed possibly causes contradict between duty cycles in the common leg. When the speed of rotor 1 is smaller than 500 r/min, the THDs in the three methods are very close at each step. However, the THD of I_{a1} in method III increases greatly when the speed is larger than 500 r/min. In method IV, it only obviously increases when larger than 800 r/min. As for the THD of I_{a2}, it increases slowly with the speed of rotor 1, mainly affected by the common leg.

Phase currents from two sets of windings both flow through the common leg in the drive. However, the phase and amplitude of phase currents in dual windings may be different due to different loads and rotor speeds. Then, the common leg current is likely not sinusoidal.

Fig. 16 shows the common leg currents and modulation signals in methods I, III, and IV. The current and modulation signals when rotor 1 runs at 300 r/min are displayed as an example. It shows common leg currents are all distorted, but their amplitudes are very similar in the three methods. As for the modulation signals, their amplitude in the common leg is not necessarily the largest. Although the speed of rotor 2 is constant, the modulation signal amplitudes of winding 2 also increase with the speed of rotor 1. It means the modulations on the two sides affect each other. In the same condition, the proposed method has the smallest modulation signals, so it has the largest linear modulation region.

B. Rotor 2 at High Speed

Then, the speed of rotor 2 increases to 400 r/min, while the speed of rotor 1 is also increased by 100 r/min at each step. Fig. 17 shows the variation of speeds and current of the machine in all methods. It can be seen that the maximum speeds of rotor 1 all decrease except for that in method II. In method II, the two sets of windings are driven separately, so the speeds of two rotors do not affect each other. In the other three methods, the maximum speeds of rotor 1 are 420, 750, and 900 r/min, respectively. The speed range of the proposed method is also much wider than that of methods I and III, although the increase in the speed of rotor 2 reduces the speed range of rotor 1. Thus, the enlargement of the modulation range is not affected by the rotor speed. Fig. 18 shows the THDs of phase currents when rotor 2 runs at 400 r/min. Apart from method II, another three methods all have larger THDs when the speed of rotor 2 is larger. The THD reaches 55.44% in method III when rotor 1 runs at 750 r/min. The THDs of I_{a2} also become larger compared with those in Fig. 15. It means the increase in the speed of one rotor can not only reduce the speed range of another rotor but also increase the THD of

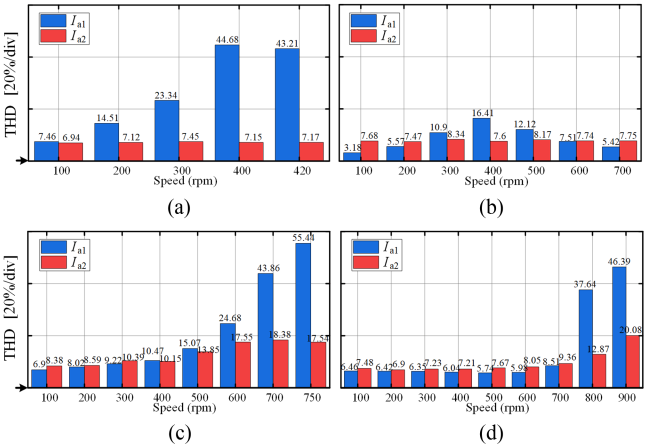

Fig. 18. THD of phase currents when rotor 2 runs at 400 r/min. (a) Method I. (b) Method II. (c) Method III. (d) Method IV.

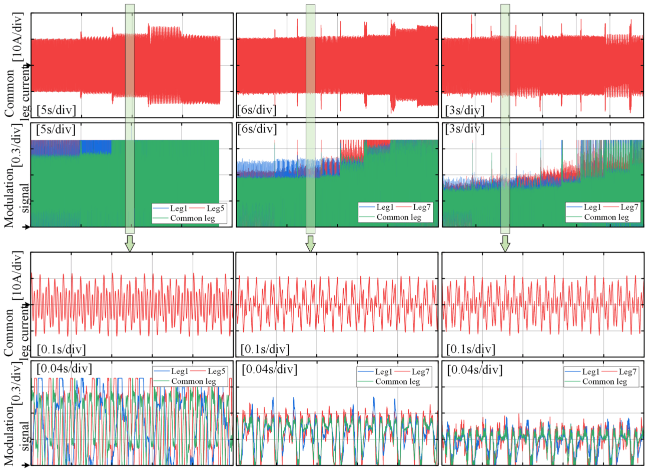

(a) (b) (c)

Fig. 19. Common leg currents and modulation signals when rotor 2 runs at 400 r/min. (a) Method I. (b) Method III. (c) Method IV.

phase currents with constant dc-bus voltage. However, compared with methods I and III, method IV nearly has the smallest THD and widest speed range. It means the contradiction between the two sets of windings in the common leg can be relieved by the proposed method.

Fig. 19 shows the common leg currents and modulation signals when rotor 2 runs at 400 r/min. The current and modulation signals when rotor 1 runs at 300 r/min are also taken as an example. Compared with the current controlled by the same method in Fig. 16, it has a different distorted waveform and a similar amplitude. The frequencies are also different. It shows different speeds can lead to different distortions in the common leg current, but the amplitude is hard to be affected. Besides, the amplitudes of the current controlled by the three methods are also the same, which means the amplitude is mainly affected by the load rather than the control method. It can be seen that the increase of rotor 2 speed makes all the modulation signals increase. When rotor 2 runs at 400 r/min, method I is overmodulated easily. Compared with Fig. 16, modulation signals have different amplitudes. Thus, the increase of either speed will increase the modulation signals. The current THDs are larger when rotor 1 runs at the same speed.

VI. CONCLUSION

This article proposes an improved PWM control method for the DSAR-AFPMM to get a wide speed range. The machine has two independent rotors and two sets of windings, so a seven-leg VSI is proposed as a reduced-switch-count SEW drive topology. It greatly enlarges the speed range of the two rotors of the machine. As for the improved PWM method, it optimizes the injected ZSC to relieve the contradiction between the duty cycles in the common leg according to the cost function. The comparison between different control methods shows the proposed method has the widest speed range. The experiment shows the THD of phase current will increase with the speed, but the improved PWM method still has the smallest THD among all the methods. It also does not add extra burden on the common leg. This method can also be applied to similar multimotor drives in addition to the proposed DSAR-AFPMM drive. It will not be affected by the machine types.

REFERENCES

[1] R. Huang, Z. Song, Z. Dong, Y. Liu, and C. Liu, “Hybrid optimization and comparative analysis of a novel double-side asynchronous rotor axial-flux permanent magnet machine,” *IEEE Trans. Transp. Electrific.*, vol. 10, no. 2, pp. 3373–3382, Jun. 2024, doi: 10.1109/TTE.2023.3303047.

[2] Z. Zeng, C. Zhu, X. Jin, W. Shi, and R. Zhao, “Hybrid space vector modulation strategy for torque ripple minimization in three-phase four-switch inverter-fed PMSM drives,” *IEEE Trans. Ind. Electron.*, vol. 64, no. 3, pp. 2122–2134, Mar. 2017, doi: 10.1109/TIE.2016.2625768.

[3] W. Wang, Z. Jinghao, and M. Cheng, “A dual-level hysteresis current control for one five-leg VSI to control two PMSMs,” *IEEE Trans. Power Electron.*, vol. 32, no. 1, pp. 804–814, Jan. 2017, doi: 10.1109/TPEL.2016.2535294.

[4] C. B. Jacobina, E. C. d. Santos, E. R. C. d. Silva, M. B. d. R. Correa, A. M. N. Lima, and T. M. Oliveira, “Reduced switch count multiple three-phase AC machine drive systems,” *IEEE Trans. Power Electron.*, vol. 23, no. 2, pp. 966–976, Mar. 2008, doi: 10.1109/TPEL.2007.915027.

[5] S. N. Vukosavic, M. Jones, D. Dujic, and E. Levi, “An improved PWM method for a five-leg inverter supplying two three-phase motors,” in *Proc. IEEE Int. Symp. Ind. Electron.*, 2008, pp. 160–165, doi: 10.1109/ISIE.2008.4676881.

[6] Y. S. Lim, J. S. Lee, and K. B. Lee, “Advanced speed control for a five-leg inverter driving a dual-induction motor system,” *IEEE Trans. Ind. Electron.*, vol. 66, no. 1, pp. 707–716, Jan. 2019, doi: 10.1109/TIE.2018.2831172.

[7] C. S. Lim, E. Levi, M. Jones, N. A. Rahim, and W. P. Hew, “A fault-tolerant two-motor drive with FCS-MP-based flux and torque control,” *IEEE Trans. Ind. Electron.*, vol. 61, no. 12, pp. 6603–6614, Dec. 2014, doi: 10.1109/TIE.2014.2317135.

[8] W. Wang, Z. Lu, W. Hua, Z. Wang, and M. Cheng, “Dual-level located feedforward control for five-leg two-mover permanent-magnet linear motor traction systems,” *IEEE Trans. Power Electron.*, vol. 35, no. 12, pp. 13673–13686, Dec. 2020, doi: 10.1109/TPEL.2020.2995241.

[9] Y. Kimura, M. Hizume, and K. Matsuse, “Independent vector control of two PM motors with five-leg inverter by the expanded two-arm modulation method,” in *Proc. Eur. Conf. Power Electron. Appl.*, Dresden, Germany, 2005, pp. 1–7, doi: 10.1109/EPE.2005.219400.

[10] W. Wang, J. Zhang, M. Cheng, and R. Cao, “Direct torque control of five-leg dual-PMSM drive systems for fault-tolerant purposes,” *J. Power Electron.*, vol. 17, no. 1, pp. 161–171, 2017.

[11] D. Dujic, M. Jones, S. N. Vukosavic, and E. Levi, “A general PWM method for a (2n + 1) -leg inverter supplying n three-phase machines,” *IEEE Trans. Ind. Electron.*, vol. 56, no. 10, pp. 4107–4118, Oct. 2009, doi: 10.1109/TIE.2009.2014909.

[12] Q. Geng, Z. Li, M. Zhang, Z. Zhou, H. Wang, and T. Shi, “Sensorless control method for dual permanent magnet synchronous motors driven by five-leg voltage source inverter,” *IEEE J. Emerg. Sel. Topics Power Electron.*, vol. 10, no. 1, pp. 260–272, Feb. 2022, doi: 10.1109/JESTPE.2021.3096198.

[13] Y. Chen, C. Liu, S. Liu, and Y. Liu, “Predictive control scheme with adaptive overmodulation for a five-leg VSI driving dual PMSMs,” *IEEE Trans. Ind. Electron.*, vol. 71, no. 1, pp. 71–81, Jan. 2024, doi: 10.1109/TIE.2023.3245221.

[14] Z. Song, C. Liu, Z. Dong, and R. Huang, “Improved multi-stage decoupling space vector modulation for asymmetrical multiphase PMSM with series winding connection,” *IEEE Trans. Power Electron.*, vol. 37, no. 9, pp. 10951–10966, Sep. 2022, doi: 10.1109/TPEL.2022.3163275.

[15] R. Huang, Z. Dong, B. Zhang, and C. Liu, “Decoupled modulation strategy for harmonic current suppression in five-phase series-end winding PMSM drives,” *IEEE Trans. Ind. Electron.*, vol. 71, no. 10, pp. 13480–13485, Oct. 2024, doi: 10.1109/TIE.2024.3349582.

[16] A. Li, D. Jiang, Z. Liu, X. Sun, and W. Kong, “Unified analysis of winding connection sequence in series-end winding topology,” *IEEE Trans. Ind. Appl.*, vol. 57, no. 1, pp. 516–527, Jan./Feb. 2021, doi: 10.1109/TIA.2020.3032936.

[17] Z. Dong, R. Huang, C. Liu, and Z. Chen, "Active zero-sequence current suppression-based model predictive current control for series-end winding PMSM drives," in *Proc. IEEE Int. Conf. Predictive Control Elect. Drives Power Electron.*, 2023, pp. 1–6, doi: 10.1109/PRECEDE57319.2023.10174405.

[18] S. Liu, Y. Liu, B. Zhang, and C. Liu, "Full-speed region predictive current control method of symmetrical series-winding PMSM with higher DC-link utilization," *IEEE Trans. Ind. Electron.*, vol. 71, no. 6, pp. 5541–5552, Jun. 2024, doi: 10.1109/TIE.2023.3292867.

[19] A. Li, D. Jiang, L. Zicheng, and W. Kong, "Five-phase series-end winding motor controller: Converter topology and modulation method," in *Proc. IEEE Energy Convers. Congr. Expo.*, 2019, pp. 629–634, doi: 10.1109/ECCE.2019.8912165.

[20] A. Li, D. Jiang, Z. Liu, and X. Sun, "Generalized PWM method for series-end winding motor drive," *IEEE Trans. Power Electron.*, vol. 36, no. 4, pp. 4452–4462, Apr. 2021, doi: 10.1109/TPEL.2020.3024591.

[21] X. Sun, Z. Liu, A. Li, Z. Wang, D. Jiang, and R. Qu, "Self-adaptive fault-tolerant control of three-phase series-end winding motor drive," *IEEE Trans. Power Electron.*, vol. 37, no. 9, pp. 10939–10950, Sep. 2022, doi: 10.1109/TPEL.2022.3160747.

[22] R. Huang, B. Zhang, Y. Liu, and C. Liu, "Investigation of magnetic isolation in a double-side asynchronous rotor-AFPM machine based on harmonic analysis," *IEEE Trans. Ind. Electron.*, to be published, doi: 10.1109/TIE.2024.3417985.

[23] Z. Keliang and W. Danwei, "Relationship between space-vector modulation and three-phase carrier-based PWM: A comprehensive analysis [three-phase inverters]," *IEEE Trans. Ind. Electron.*, vol. 49, no. 1, pp. 186–196, Feb. 2002, doi: 10.1109/41.982262.

Rundong Huang (Member, IEEE) received the B.Eng. degree in hydropower engineering, and the M.Eng. degree in electrical engineering from Huazhong University of Science and Technology, Wuhan, China, in 2017 and 2020, respectively. He is currently working toward the Ph.D. degree in electrical and electronic engineering with the City University of Hong Kong, Hong Kong.

His current research interests include the design, analysis, and optimization of axial-flux permanent-magnet machines, control and drive of electric machines, electric machines for propulsion systems and actuators, and analytical methods for electric machines.

Chunhua Liu (Senior Member, IEEE) received the B.Eng. and M.Eng. degrees in automatic control from Beijing Institute of Technology, Beijing China, and Ph.D. degree in electrical and electronic engineering from The University of Hong Kong, Hong Kong, in 2002, 2005, and 2009, respectively.

Since 2015, he has been with City University of Hong Kong, Hong Kong, where he is currently a Professor in electrical and electronic engineering with the School of Energy and Environment. In these areas, he has authored or coauthored more than 300 refereed papers. His research interests include electric machines and drives, electric vehicles and aircrafts, electric robotics and ships, renewables and microgrids, power electronics and wireless power transfer.

Dr. Liu is currently an Associate Editor for IEEE TRANSACTIONS ON INDUSTRIAL ELECTRONICS, an Editor for IEEE TRANSACTIONS ON VEHICULAR TECHNOLOGY, an Editor for IEEE TRANSACTIONS ON ENERGY CONVERSION, and an Editor for IEEE POWER ENGINEERING LETTERS. Also, he is an Editor for *Energies*, a Subject Editor for *IET–Renewable Power Generation*, an Associate Editor for *Open Journal of the Industrial Electronics Society*, an Associate Editor for IEEE ACCESS; an Associate Editor for IEEE CHINESE JOURNAL OF ELECTRICAL ENGINEERING, an Associate Editor for *CES Transactions on Electrical Machines and Systems*, an Associate Editor fot *Elsevier Green Energy and Intelligent Transportation*, and an Editor for IEEE Transactions on Magnetics–Conference, respectively. In addition, he is the Chair and Founder of both Hong Kong Chapter, IEEE Vehicular Technology Society, and Hong Kong and Guangzhou Joint Chapter, IEEE Industrial Electronics Society, respectively. In addition, he was a RGC Research Fellow by the HKRGC, a Distinguished Lecturer for IEEE Vehicular Technology Society, and recognized among the top 2% of the world's most highly cited scientists in reports by Elsevier and Stanford University since 2020.